Available online at www.sciencedirect.com

ScienceDirect

Acta Materialia 76 (2014) 94–105

Acta MATERIALIA

www.elsevier.com/locate/actamat

Designing Heusler nanoprecipitates by elastic misfit stabilization in Fe–Mn maraging steels

J. Millán [a,c], S. Sandlöbes [a,*], A. Al-Zubi [b,d], T. Hickel [b], P. Choi [a], J. Neugebauer [b], D. Ponge [a], D. Raabe [a]

[a] Max-Planck-Institut für Eisenforschung GmbH, Department for Microstructure Physics and Alloy Design, Max-Planck-Str. 1, 40477 Düsseldorf, Germany
[b] Max-Planck-Institut für Eisenforschung GmbH, Department for Computational Materials Design, Max-Planck-Str. 1, 40477 Düsseldorf, Germany
[c] Universidad Simón Bolívar, Departamento de Ciencia de los Materiales, Valle de Sartenejas, Baruta 1086, Estado Miranda, Caracas, Venezuela
[d] Peter Grünberg Institut and Institute of Advanced Simulation, Forschungszentrum Jülich and JARA, D-52425 Jülich, Germany

Received 22 November 2013; accepted 6 May 2014

Abstract

B2 NiMn and Ni_2MnAl Heusler nanoprecipitates are designed via elastic misfit stabilization in Fe–Mn maraging steels by combining transmission electron microscopy (TEM) correlated atom probe tomography (APT) with ab initio simulations. Guided by these predictions, the Al content of the alloys is systematically varied, and the influence of the Al concentration on structure stability, size and distribution of precipitates formed during ageing at 450 °C is studied using scanning electron microscopy–electron backscatter diffraction, TEM and APT. Specifically, the Ni_2MnAl Heusler nanoprecipitates exhibit the finest sizes and highest dispersion and hence lead to significant strengthening. The formation of the different types of precipitates and their structure, size, dispersion and effect on the mechanical properties of the alloys are discussed.
© 2014 Acta Materialia Inc. Published by Elsevier Ltd. All rights reserved.

Keywords: Heusler nanoprecipitates; Maraging TRIP steels; Atom probe tomography; Transmission electron microscopy; Ab initio predictions

1. Introduction

Maraging steels combine ultra-high strength and high fracture toughness by hardening a carbon-free martensitic matrix with nanosized intermetallic precipitates [1]. Typical applications lie in aerospace and manufacturing, where minimum weight at maximum reliability is essential [1]. This is achieved through high dispersion of precipitates, e.g. Ni_3Ti intermetallics, which requires alloying with a large amount of Ni, typically in the range of 18 wt.% [2–5].

The approach in the present study is to apply a maraging treatment [6] to martensitic Fe–Mn alloys with significantly reduced Ni content to obtain ultra-high strength at sufficient ductility yet lean alloy composition [7,8]. As reported earlier [7–9], further remarkable improvement in toughness and ductility in Fe–Mn alloys can be obtained via partial re-austenitization.

A high Mn content of 6–12 wt.% allows reduction of the Ni content to <5 wt.% (and other elements if necessary) and promotes precipitation by providing high supersaturation [8,9].

The modified material strategy gives access to new intermetallic phases combining Ni and Mn, such as NiMn or the Heusler phase Ni_2MnAl. NiMn can form with B2 and Ni_2MnAl with either $L2_1$ or B2 structure [10,11]. As both structures are ordered phases on the same body-centred cubic (bcc) lattice as the surrounding bulk solid solution martensite, coherency between matrix and particles is possible. This leads to a low nucleation energy,

* Corresponding author.
E-mail address: s.sandloebes@mpie.de (S. Sandlöbes).

http://dx.doi.org/10.1016/j.actamat.2014.05.016
1359-6454/© 2014 Acta Materialia Inc. Published by Elsevier Ltd. All rights reserved.

enabling a very fine distribution in the bcc matrix via homogeneous nucleation.

The NiMn or Ni_2MnAl precipitates have a much lower Ni content than Ni_3Ti and, for nucleation of these precipitates (NiMn, Ni_2MnAl), much lower Ni activity in the matrix is required, enabling a new generation of lean maraging steels.

This study employs high resolution experimental characterization methods (atom probe tomography (APT) and transmission electron microscopy (TEM)) in combination with ab initio predictions to design lean maraging TRIP steels reinforced by highly dispersed NiMn or Ni_2MnAl Heusler nanoprecipitates.

2. Experimental methodology

2.1. Alloy production

The alloys were cast into round 1 kg billets in a vacuum induction furnace. In order to homogenize the microstructure and remove segregation, two cycles consisting of re-austenitization and hot deformation were conducted. Additionally, deformation by cold rolling was applied, and subsequent recrystallization and solution heat treatment were performed in an argon atmosphere at 1050 °C for 0.5 h followed by water quenching. Final ageing heat treatment was conducted at 450 °C for 65 h. Further synthesis and processing details are given in Refs. [7–9].

As discussed below, the chemical compositions of the alloys were designed by an optimization routine including insights of ab initio calculations (Table 1).

2.2. TEM specimen preparation

Discs 3 mm in diameter and 1 mm thick were cut via wire erosion. They were mechanically ground to 70–90 μm thickness, followed by electro-polishing until perforation (Struers Tenupol-5). The electrolyte was a solution of 10 vol.% perchloric acid and 90 vol.% ethanol for MA_L_Al, MA_H_Al, MA_M_Al alloys and 6 vol.% perchloric acid, 30 vol.% 1-butonalglycolester and 64 vol.% methanol for the M_L_Al and M_H_Al alloys (reference alloys). Specimen nomenclature is given in Table 1. This means that the abbreviation MA_L_Al stands for a material with martensitic–austenitic matrix with a low Al content according to Table 1. TEM observations were performed using a Philips CM20 with LaB_6 filament at an acceleration voltage of 200 kV.

2.3. APT specimen preparation

Atomic-scale chemical analysis of the material after ageing was conducted using APT [12–15]. Specimens were prepared by a two-step electrochemical polishing method [9]. Square rods 0.3×0.3 mm^2 in cross section and 20 mm long were cut from the aged samples. In the first electrochemical polishing step, the square rods were roughly sharpened using a solution of 9 vol.% perchloric acid in glacial acetic acid. The second step was done in a solution of 2 vol.% perchloric acid in butoxyethanol. Final sharpening by ion milling using a dual focused ion beam microscope (FEI Helios Nanolab 600 dual-beam FIB) was carried out in order to obtain an initial radius of the samples <50 nm [16]. Pulsed laser APT was performed using a local electrode atom probe (LEAP 3000X HR™, Imago Scientific Instruments) at a specimen temperature of ~64 K. The laser pulse energy was set to 0.4 nJ with a constant pulse frequency of 250 kHz [17,18]. The average detection rate amounted to 5 atoms per 1000 pulses. Data analysis was performed using the IVAS® software provided by Imago Scientific Instruments. For the atomic reconstructions, an evaporation field constant of 33 V nm^{-1}, which corresponds to Fe at 77 K, was employed [9].

3. Theoretical methodology

Ab initio calculations were performed for the martensitic matrix and the relevant precipitate phases, using density functional theory (DFT) in the generalized gradient approximation [19]. The VASP package [20] with the projector augmented wave method [21] was used to calculate the total energies of these systems. An energy cutoff of 350 eV and a smearing parameter of 0.2 eV were chosen. Different supercell sizes ranging from a two-atomic $1 \times 1 \times 1$ cell (B2 NiMn phase), via a $2 \times 2 \times 2$ cell ($L2_1$ Ni_2MnAl phase) up to a $3 \times 3 \times 3$ cell (ferritic matrix) were used, guaranteeing an equivalent k-point mesh in all

Table 1
Chemical compositions of the alloys produced (in wt.%[a]).

Alloy[b]	C	Mn	Ni	Al	Ti	Mo	Si	S	P	O	N
Maraging TRIP steels											
MA_L_Al	0.0124	12.2	2.01	0.143	1.07	1.09	0.054	–	–	0.0048	0.0037
MA_M_Al	0.0124	12.1	2.95	0.75	<0.001	<0.002	0.0078	0.0061	<0.002	0.0011	0.0030
MA_H_Al	0.0158	11.8	3.00	1.28	0.001	0.0015	0.0058	0.0062	–	<0.002	0.0025
Reference alloys											
M_L_Al	0.0056	9.10	1.97	0.155	1.02	1.08	0.044	0.0026	<0.001	<0.002	0.0006
M_H_Al	0.0106	8.76	2.98	1.33	<0.001	<0.002	0.0087	0.0052	<0.002	<0.001	0.0048

[a] Conversion from wt.% to at.% for the steels investigated: Fe, Mn, at.% = wt.%; Ni, at.% = 0.93 × wt.%; Al, at.% = 2.02 × wt.%.
[b] Nomenclature: M, martensite matrix; A, austenite; MA, martensite plus austenite matrix; L, low content; M, medium content; H, high content; Al, aluminium.

simulations. The calculations were performed for different types of magnetic ordering, specified below. Taking into account the fact that ageing was performed at 450 °C (i.e. below the Curie temperature of the martensite matrix), the magnetic structure with the lowest energy was used for the evaluation. In some calculations chemical disorder of the matrix atoms has been considered using a special quasi-random structure (SQS) [22] for a $2 \times 2 \times 2$ supercell, for which the ATAT package was employed [23,24]. Temperature effects due to lattice vibrations, electronic and magnetic excitations are subject to further investigations and are not considered here.

Chemical equilibrium between the matrix and the precipitate was ensured within a grand canonical ensemble. This requires the knowledge of the chemical potentials for the alloying elements in order to calculate the formation enthalpies of the precipitate phases via

$$\Delta H^{\mathrm{f}}_{\mathrm{NiMn}} = E[\mathrm{NiMn}] - \mu_{\mathrm{Ni}} - \mu_{\mathrm{Mn}}$$

and

$$\Delta H^{\mathrm{f}}_{\mathrm{Ni_2MnAl}} = E[\mathrm{Ni_2MnAl}] - 2\mu_{\mathrm{Ni}} - \mu_{\mathrm{Mn}} - \mu_{\mathrm{Al}}$$

where $H^{\mathrm{f}}_{\mathrm{Y}}$ is the formation enthalpy of Y, E[Y] is the energy per formula unit of Y, and μ_{X} is the chemical potential of the element X.

The chemical potentials are determined from the solution enthalpy and the concentration of these elements in the Fe matrix. The former values were obtained from ab initio calculations, whereas the latter were adjusted to the chemical compositions given in Table 1. Assuming a dilute limit and performing calculations in a 54 atom supercell, the following relation was used for the concentration c(X) of an element X:

$$c(\mathrm{X}) = \exp[-(E[\mathrm{Fe_{53}X}] - 53E[\mathrm{Fe}] - \mu_{\mathrm{X}})/k_{\mathrm{B}}T]$$

where k_{B} is the Boltzmann constant, and T is the temperature (an ageing temperature of 450 °C was used according to the experiments).

4. Experimental results

4.1. Precipitation hardened maraging TRIP steels

Fig. 1 shows electron-backscatter diffraction (EBSD) images of the microstructures of the MA_L_Al, MA_H_Al and MA_M_Al alloys. The phase distribution maps (bottom row maps) show that the material is composed of α' martensite and γ austenite. Owing to the ultra-fine grain structure of the α' martensite, overlapping patterns are partially incorrectly indexed as ε martensite. The average grain and lath size in these alloys is lower than the excitation volume during EBSD, and overlapping patterns were therefore obtained and wrongly indexed as hexagonal close packed by the automatic detection software. In the undeformed material, no evidence for ε martensite was found in EBSD when applying a smaller EBSD step size, in agreement with X-ray diffraction (XRD) and TEM analyses. The inverse pole figure maps (upper image row) reveal the ultra-fine structure of the α' martensite.

TEM (left image row in Fig. 2) and APT (right image row) analyses of MA_L_Al, MA_H_Al and MA_M_Al alloys reveal the existence of nanosized precipitates in the α' martensite in all three alloys. The austenite is free of precipitates.

In the APT elemental maps, the iso-concentration surfaces of 10 at.% Ni are shown in green. The value of 10 at.% Ni was chosen as a threshold value to distinguish matrix from precipitates. Ni and Mn atoms in the matrix are shown by green and yellow dots, respectively.

Both characterization methods show that, under the same ageing condition (450 °C/65 h), precipitates of different sizes and dispersion are formed in the different alloys. Here, a clear trend is observed, namely, precipitate size and dispersion coarsening with decreasing Al content. In the alloy with the lowest Al concentration (MA_L_Al, 0.14 wt.% Al), the largest precipitates with an average size of 10–20 nm and the coarsest dispersion are formed (Fig. 2a–c), while the alloy with the highest Al content (MA_H_Al, 1.28 wt.% Al) exhibits the smallest precipitate size of 3–5 nm and the finest precipitate dispersion (Fig. 2g–i). MA_M_Al has a medium Al content of 0.75 wt.% and has medium sized (5–10 nm average size) and medium dispersed precipitates (Fig. 2d–f).

The crystal structures of the precipitates were investigated using selected area diffraction patterns (SADP); see the insets in the TEM micrographs shown in Fig. 2. The left-hand side images show SADP of $[0\,0\,1]_{\mathrm{bcc}}$ pole orientations, and the right-hand side a row of $[0\,1\,1]_{\mathrm{bcc}}$ pole orientations (each of the same position in the same grain) for (a) MA_L_Al, (d) MA_M_Al and (g) MA_H_Al, respectively. The SADP taken in the bcc matrix reveal that the distortion of the α' martensite is small because of the applied maraging treatment.

It was observed that the precipitates have either B2 or $L2_1$ structure. Owing to chemical ordering, $L2_1$ structured precipitates exhibit $[1\,1\,1]_{\mathrm{L21}}$ reflexes, which are visible in the $[0\,1\,1]_{\mathrm{bcc}}$ orientation. B2 structured precipitates do not exhibit these [1 1 1] reflexes. It was observed that, in MA_H_Al (Fig. 2g) and MA_M_Al (Fig. 2d) alloys, precipitates of both $L2_1$ and B2 structures are formed. In the MA_M_Al alloy, the amount of $L2_1$ and B2 precipitates seems to be similar, whereas in the MA_H_Al alloy, the amount of $L2_1$ is higher (as can be concluded from the relative intensities of $L2_1$ and B2 spots). The dark-field TEM micrograph shown in Fig. 2g was taken using a $L2_1$ [1 1 1] spot. The MA_L_Al alloy (Fig. 2a) contains only B2 phase precipitates. The streaking of the super lattice spots indicates that the precipitates have a platelet shape. Both precipitate types (B2 and $L2_1$ structure) are coherent with the [0 0 1] planes of the α' martensite (bcc) matrix. Different orientational variants of the precipitates along the different $[0\,0\,1]_{\mathrm{bcc}}$ planes are visible in the $[0\,1\,1]_{\mathrm{bcc}}$ SADP. It is obvious from the $[0\,1\,1]_{\mathrm{bcc}}$ SADP that the $L2_1$ phase precipitates

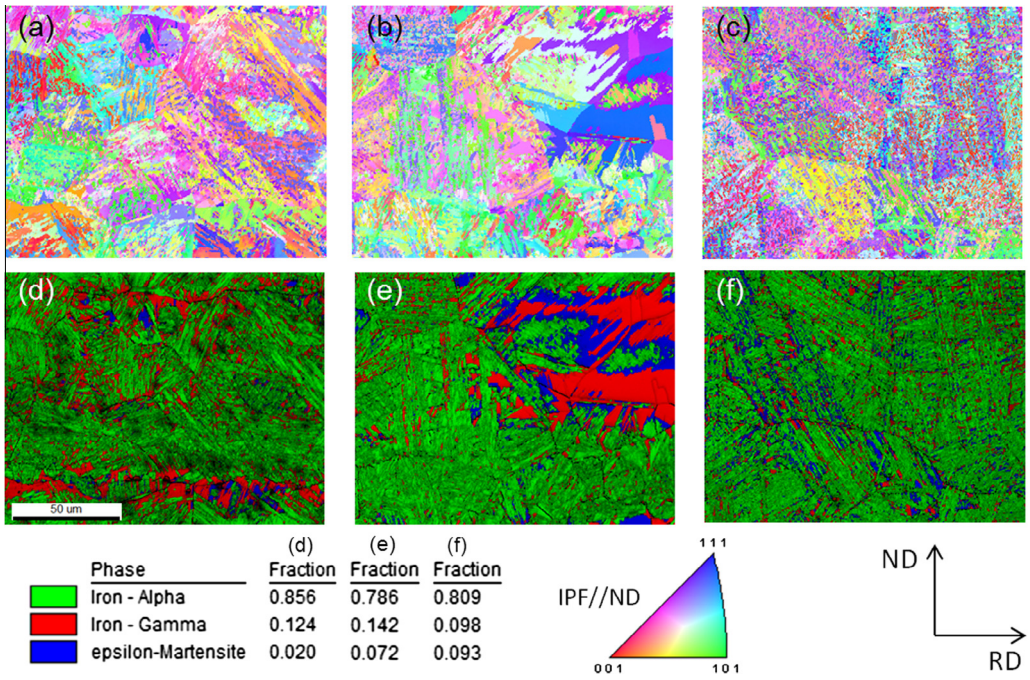

Fig. 1. EBSD results of the 450 °C/65 h aged alloys. (a), (b) and (c) represent the inverse pole figures (IPF), showing the crystallographic orientations in terms of ⟨**uvw**⟩ vectors parallel to the normal direction of the alloys: (a) MA_L_Al; (b) MA_M_Al; (c) MA_H_Al, respectively; (c–e) show the corresponding phase distribution maps.

have a lower mismatch to the surrounding bcc matrix than the B2 phase precipitates.

To determine the chemical composition of the precipitates in the alloys, further APT analysis was performed. The average concentrations over all precipitates in the analysed sample volumes were determined. Fig. 2 shows the resulting concentration profiles of the precipitates in MA_L_Al (Fig. 2c), MA_H_Al (Fig. 2f) and MA_M_Al (Fig. 2i). These analyses reveal that the precipitates have different Mn and Al concentrations: The precipitates formed in MA_L_Al alloy have an average chemical composition of 50 at.% Ni, 35 at.% Mn, 2.5 at.% Al and 5 at.% Ti (balance Fe). In MA_H_Al, precipitates with average concentrations of 50 at.% Ni, 20 at.% Mn and 20 at.% Al (balance Fe) are formed, and the precipitates in MA_M_Al have an average chemical composition of 50 at.% Ni, 28 at.% Mn and 18 at.% Al (balance Fe). The chemical fractions of the precipitates indicate that, in MA_L_Al alloy, NiMn particles are precipitated, in MA_H_Al Ni_2MnAl precipitates are formed, and in MA_M_Al both NiMn and Ni_2MnAl are precipitated.

Fe ions, which are observed in the precipitates of all three alloys, might originate from different effects: (i) reconstruction artefacts due to local magnification effects; (ii) (mis)identification as a result of the ionic trajectory overlap during the field evaporation process and the significant Al^{+}/Fe^{2+}overlapped signal in the mass-to-charge spectra; and (iii) substitutional Fe in the precipitates as a result of high chemical activity of Fe in the alloys. More details about these aspects have been published elsewhere [25]. Quantification of these different effects is not possible within APT.

The combined TEM and APT analysis reveals that a low Al content (MA_L_Al; 0.14 wt.% Al) leads to precipitation of NiMn with B2 structure, and a high Al content (MA_H_Al; 1.3 wt.% Al) causes the formation of Ni_2MnAl precipitates with $L2_1$ and B2 structure during ageing at 450 °C. Medium Al alloying (MA_M_Al; 0.75 wt.% Al) supports formation of both types of precipitates during ageing.

4.2. Reference materials

In the maraging TRIP steels MA_L_Al, MA_H_Al and MA_M_Al, the strengthening effect associated with the precipitates in the martensite is counteracted by the formation of softer, reverted austenite during ageing [7,9]. Therefore, a separate investigation of the influence of the precipitates on the mechanical properties of the martensite was performed on pure martensitic reference materials. The chemical compositions of the reference steels are given in Table 1. Owing to lower Mn alloying of the 9 wt.% Mn steel (which corresponds to the Mn concentration of the martensite in the maraging TRIP steels: see Fig. 2), no retained austenite was present in these materials after quenching, and no reverted austenite was detected after ageing at 450 °C for 65 h. XRD and EBSD analyses were performed, showing purely martensitic microstructures also after ageing. The reference steels represent the two cases with low (0.15 wt.% Al: NiMn precipitates) and high (1.3 wt.% Al: Ni_2MnAl precipitates) Al alloying. The other alloying elements were not changed with respect to MA_L_Al and MA_H_Al.

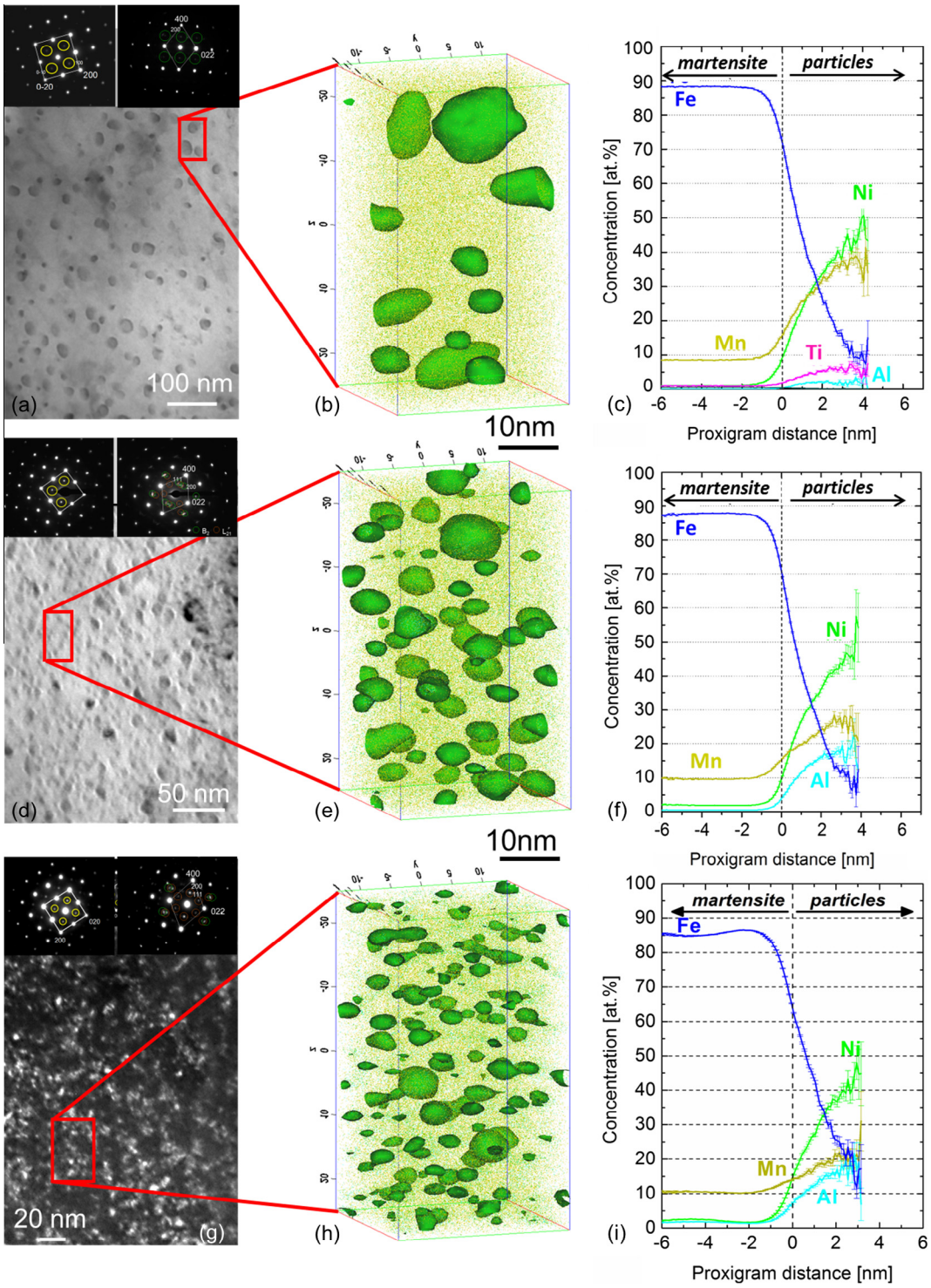

Fig. 2. (a, b, d, e, g, h) TEM images and APT reconstructions showing size and spatial distribution of the nanosized precipitates in the martensitic matrix after ageing at 450 °C for 65 h: (a, b) MA_L_Al; (d, e) MA_M_Al; (g, h) MA_H_Al alloy. Insets in the TEM micrographs show TEM SADP of $[0\,0\,1]_{bcc}$ (left) and $[0\,1\,1]_{bcc}$ (right) orientations showing superlattice reflexes from the precipitates. From the $[0\,1\,1]_{bcc}$ SADP, it is revealed that the precipitates in MA_L_Al have B2 structure, while the precipitates in MA_M_Al and MA_H_Al are of B2 as well as $L2_1$ structure. (c, f, i) Average chemical composition gradients between martensitic matrix and precipitates as derived from the proximity histogram method [25] (alloys aged at 450 °C for 65 h): (c) MA_L_Al; (f) MA_M_Al; (i) MA_H_Al.

The EBSD images in Fig. 3 show the fully martensitic microstructures of the two reference steels, M_L_Al and M_H_Al. To probe the strengthening effects of the different precipitates, hardness tests were performed after different ageing times (Fig. 4). The curves show that M_H_Al exhibit much stronger age-hardening than M_L_Al.

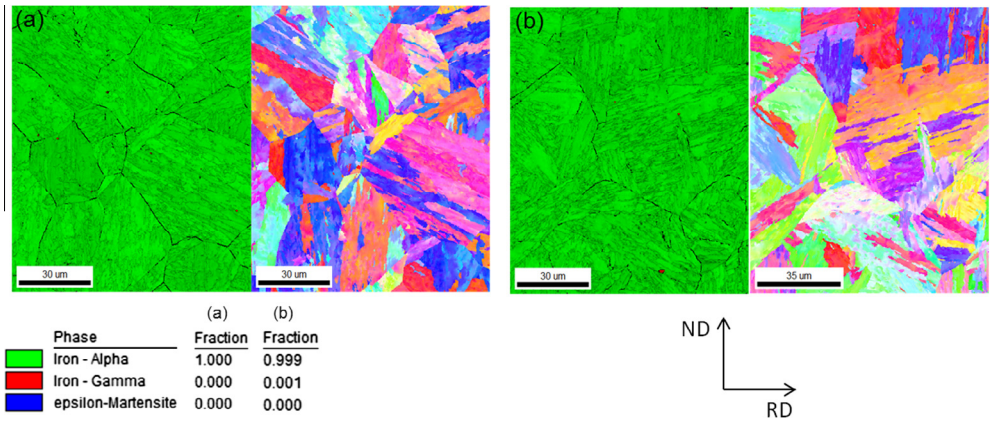

Fig. 3. EBSD results of the reference alloys (a) M_L_Al and (b) M_H_Al in aged condition: left micrographs, 450 °C for 65 h; right micrographs, phase distribution maps. IPF showing the crystallographic orientations in terms of ⟨**uvw**⟩ vectors parallel to the normal direction.

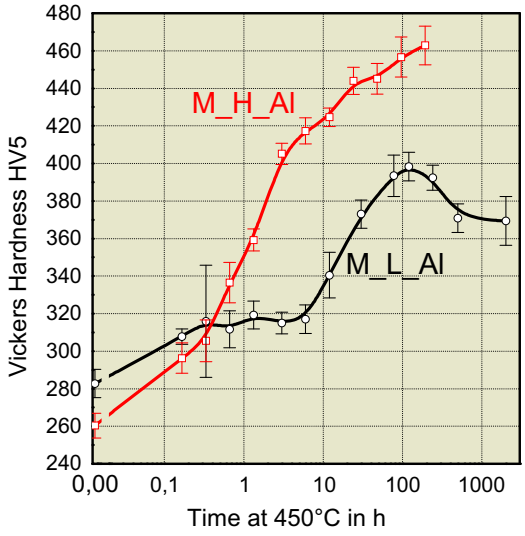

Fig. 4. Hardening response as a function of the holding time at 450 °C of the reference martensitic steels, M_L_Al (black curve) and M_H_Al (red curve). (For interpretation of the references to color in this figure legend, the reader is referred to the web version of this article.)

TEM and APT characterization of the structure and composition of the precipitates in the martensitic reference steels M_L_Al (Fig. 5a–c) and M_H_Al (Fig. 5d–f)) were performed. These analyses reveal the formation of NiMn precipitates with a B2 structure in the low Al (0.15 wt.%) containing steel M_L_Al and the formation of Ni_2MnAl precipitates with $L2_1$ and B2 structures in the high Al (1.3 wt.%) alloyed steel M_H_Al. The dark-field TEM micrograph shown in Fig. 5d was taken using a $L2_1$ [1 1 1] spot. As already found in the maraging TRIP steels (Fig. 2), the smallest particle size and the finest particle dispersion is observed for the alloy with Ni_2MnAl precipitates (Fig. 5d–f).

5. Theoretical results

The goal of ab initio calculations was to predict under which conditions the finer dispersed Ni_2MnAl precipitates form. For this purpose, the energy values of the chemical components in the different phases – the precipitates and the matrix – were calculated and compared. The evaluation was performed in two steps: First, the different phases were treated individually and, second, the results of these calculations were used to determine the formation enthalpies in thermodynamic equilibrium.

The ab initio calculation gives access not only to enthalpies, but also to structural and magnetic data of the individual phases. The calculations for the bcc matrix were performed for pure Fe as well as an Fe–Mn alloy with 12 at.% Mn, for which the chemical disorder was treated in a SQS structure. While pure Fe shows a ferromagnetic (FM) order, the magnetic alignment of the Mn atoms within this matrix depends on the Mn–Mn separation spacing. The impact of Mn on structural properties, however, is negligible. The DFT calculations provide for pure Fe a lattice constant of 2.834 Å and for the Fe–12Mn alloy 2.829 Å. Thus, it is assumed that Mn alloying up to 12 at.% has no significant effect on the lattice constant. It was also observed experimentally that Mn additions up to 20 wt.% have almost no influence on the lattice constants [26–28].

Based on this information, the lattice misfit between the precipitate phases B2–NiMn and $L2_1$–Ni_2MnAl and the bcc matrix with respect to the [0 0 1] interface was calculated (Fig. 6). Both phases have a larger equilibrium lattice constant than the matrix, giving rise to an elastic misfit parameter δ of 3% for NiMn and 2% for Ni_2MnAl. The experimentally observed coherency for small precipitates, therefore, results in elastic misfit strains. Owing to the small size of the precipitates, the absence of misfit dislocations in the matrix is assumed and the (then compressive) elastic coherency strain is attributed only to the precipitate phases during nucleation. The larger mismatch of NiMn also yields larger strain energy under elastic coherency conditions. It is interesting to note that this amount is reduced by a magneto-elastic coupling effect, which involves a magnetic phase transition within the precipitate to an antiferromagnetic (AFM) configuration under these constraints.

The thermodynamic equilibrium between the matrix and the precipitate phases is evaluated in the grand canonical

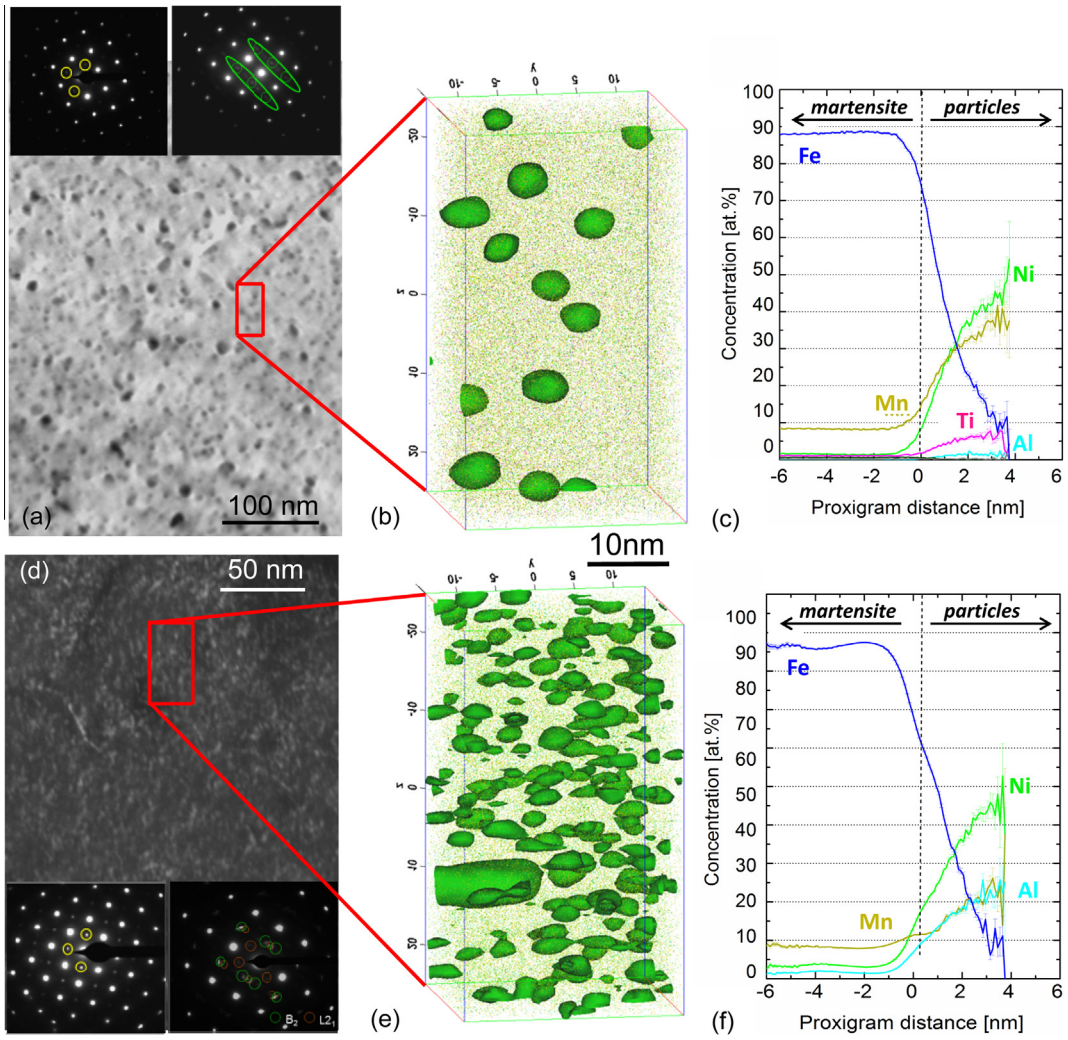

Fig. 5. (a, b, d, e) TEM images and APT reconstruction of the martensitic reference alloys in the 450 °C/65 h aged condition: (a, b) M_L_Al and (d, e) M_H_Al. Nanosized precipitates are highlighted by 10 at.% Ni iso-concentration surfaces (green). The inset in the TEM micrographs show TEM–SADP of $[0\,0\,1]_{bcc}$ and $[0\,1\,1]_{bcc}$ orientations revealing superlattice reflexes from the precipitates. From the $[0\,1\,1]_{bcc}$ SADP, it is revealed that the precipitates in M_L_Al have B2 structure, while the precipitates in M_H_Al are of B2 and $L2_1$ structure. (c, f) Average chemical gradients between precipitates and martensitic matrix calculated via proximity histograms of (c) M_L_Al and (f) M_H_Al martensitic reference alloys after ageing at 450 °C for 65 h. (For interpretation of the references to color in this figure legend, the reader is referred to the web version of this article.)

ensemble, as described in the methods section. The calculations were performed for a fixed Mn and Ni concentration of 9 and 2.8 at.%, respectively. In contrast, the concentration of Al has been kept as a free parameter. Consequently, the formation enthalpy of B2 NiMn is a fixed quantity, while the formation enthalpy of Ni_2MnAl decreases with increasing Al content. The resulting difference for both enthalpies is plotted in Fig. 7 for two situations: On the one hand (dashed line in Fig. 7), all phases are considered at their equilibrium lattice constants, as given in Fig. 6. This corresponds to an unstrained situation, as it can only occur for incoherent precipitates. On the other hand (solid line in Fig. 7), the strained situation corresponding to the experimentally observed coherency is plotted. In both cases, a critical Al concentration can be identified, above which the formation of $L2_1$ Ni_2MnAl is energetically more favourable than that of B2 NiMn. The value is ~4.2 at.% for the incoherent and 2.4 at.% for the coherent situation.

6. Discussion

The aim of this work is a knowledge-driven adjustment of the chemical composition in low Ni alloyed maraging TRIP steels for designing and optimising nanoprecipitates for high mechanical strength. More specific, the focus is on the competition of NiMn (B2 structure) and Ni_2MnAl (B2 and $L2_1$ structures) Heusler nanosized precipitates (considering also the temperature-dependent ratio of B2/$L2_1$ in the latter case) via elastic coherency stabilization. The type and amount of substitutional elements dissolved in the martensite matrix, the chemical interaction between them, as well as the thermodynamic phase equilibria define the nature of the intermetallic phase(s) formed.

In the current case, the combined TEM–APT and DFT analysis provided clear insights into the involved hardening mechanisms in terms of the elastic misfit, the dependence of NiMn and Ni_2MnAl formation on the Al content, and the

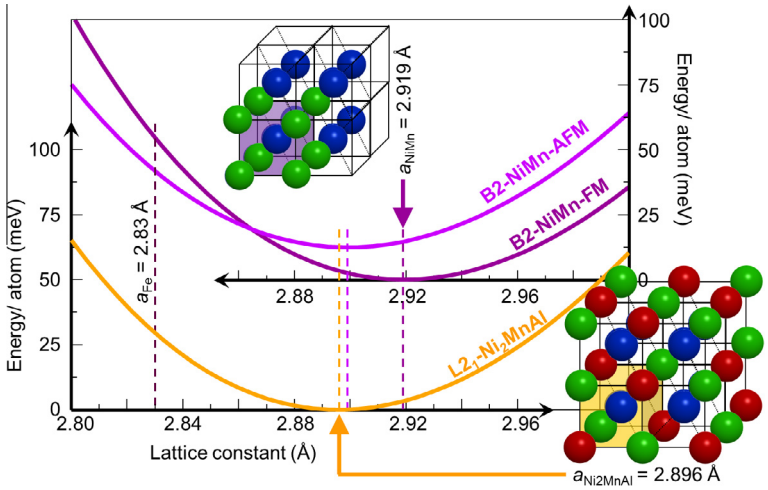

Fig. 6. Dependence of the total energies of precipitate phases B2 NiMn and $L2_1$ Ni_2MnAl on the lattice constant. All energies are plotted with respect to the energy minimum of the $L2_1$ phase. The NiMn phase has been considered both in a FM and an AFM configuration. The lattice constant of the ferritic matrix (2.83 Å) is also indicated.

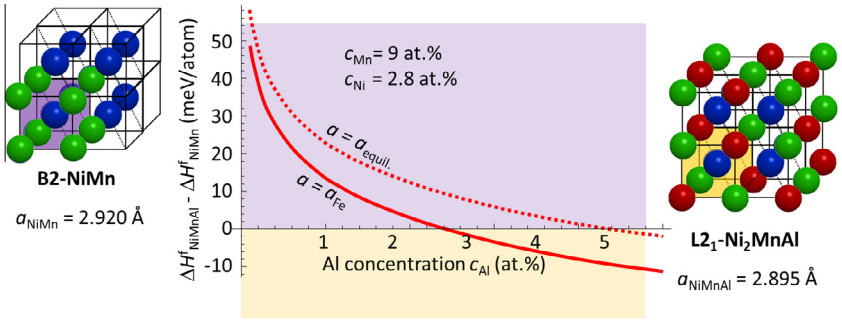

Fig. 7. Difference in the formation enthalpies of B2 NiMn and $L2_1$ Ni_2MnAl. The concentrations of Mn and Ni in the total alloy are fixed, while the concentration of Al is varied. Compared are the situations that both phases have their own equilibrium lattice constants (corresponding to incoherent precipitates, dashed line) and the situation where the precipitates are elastically constrained to match the surrounding lattice constant of the ferritic matrix (coherent precipitates, solid line). A positive difference means that NiMn is more stable, whereas a negative difference means that Ni_2MnAl is more stable.

dispersion of these precipitates. For the systematic study of these aspects, three different Al contents were compared and are discussed in the following.

6.1. Low Al alloying

The low aluminium alloy variant favours NiMn precipitates. A nominal Al content of 0.14 wt.% in the M_L_Al and MA_L_Al alloys was chosen, which is according to the ab initio predictions (Fig. 7) for 450 °C in a composition region, where the formation of $L2_1$ Ni_2MnAl is energetically less favourable than that of B2 NiMn. The correlated TEM and APT results confirm the formation of NiMn precipitates with B2 ordering (Figs. 2a and 5a).

The high content of Ni and Mn detected in the particles resembles earlier results by Singh and Wayman on the precipitation behaviour of a Fe–20Ni–5Mn alloy [29]. They attributed the age-hardening to the formation of an ordered bcc-NiMn phase during the early stages of ageing at temperatures between 350 and 450 °C, which later transforms to a disordered and more stable fcc-Ni_3Mn phase. In contrast, several authors have reported the formation of a $L1_0$ θ-NiMn intermetallic phase as responsible precipitate for age hardening in such ternary martensitic Fe–Ni–Mn alloys [30–36]. The B2 → $L1_0$ martensitic transformation occurs close to 700 °C in stoichiometric $Ni_{50}Mn_{50}$ and has been studied in bulk binary Ni–Mn alloys at compositional ranges close to stoichiometry, e.g. Refs. [37,38]. However, it is known that both Ti and Al significantly alter the structure of the face-centred tetragonal θ-NiMn phase. It has been demonstrated experimentally in binary bulk Ni–Mn alloys that Ti and Al additions significantly reduce the temperature of the $\beta \rightarrow \theta$ martensitic transformation and the tetragonality of the $L1_0$ θ-NiMn phase [39,40]. The broadening of the stability range of the B2 β-NiMn phase towards lower temperatures and the reduction of the tetragonality are expected to be due to stronger Ti–Ni and Al–Ni interactions compared with the Ni–Mn interaction. If a bulk NiMn alloy contains more than 12% Ti, the $\beta \rightarrow \theta$ martensitic transformation temperature can be lowered even below room temperature, stabilizing B2 β-NiMn in ambient conditions [10].

The present results show that, in the M_L_Al and MA_L_Al alloys, the precipitates with B2-ordered NiMn structure remain stable even after 65 h ageing at 450 °C and subsequent quenching to room temperature. No evidence of $L1_0$ ordering was encountered via TEM–SADP analysis. Besides the high concentration of Ni and Mn, there is a certain amount of Ti (5 at.%) and Al (2.5 at.%) detected in the precipitates. As mentioned above, both elements Ti and Al preferentially occupy Mn sites in the NiMn superlattice and are probably responsible for the stabilization of the B2 phase in M_L_Al and MA_L_Al at lower temperatures.

In the absence of Ti and with further increase in the nominal Al content (see Table 1), the chemistry of the nanosized particles formed during ageing is partially modified with respect to that detected in the MA_L_Al and M_L_Al alloys.

In Mn-free stainless maraging steels, the formation of Ni and Al-rich coherent zones and, in the following, the B2 intermetallic compound NiAl was observed [41–44]. Unlike those steels, which contain essentially no Mn, the Mn content in the current experimental alloys is relatively high (9 vs. 12 wt.%), resulting in the formation of NiMn and Ni_2MnAl precipitates, respectively. According to first-principles calculations performed by Kolli et al. [44], Mn preferentially occupies the Al sublattice sites in the B2–NiAl structure. These calculations were used to explain the B2–Ni(Al, Mn) phase formed heterogeneously around Cu-rich precipitates in a low-Mn Fe–Cu-based alloy aged at 500 °C. Kolli et al. [44] assumed that first B2–NiAl nucleated, followed by incorporation of Mn into the superlattice. The Mn content detected in the B2 interfacial phase was limited to 8 at.% owing to the low amount of Mn in the Fe–Cu steel [44].

6.2. High Al alloying

If the Al content exceeds the critical value derived by ab initio calculations (Fig. 7), formation of the Ni_2MnAl Heusler phase is favoured. Therefore, an Al content of 1.4 wt.% (~3 at.%) was chosen for the MA_H_Al and M_H_Al alloys. Indeed, TEM and APT analyses reveal Ni_2MnAl precipitates with an average diameter of 3–5 nm with a chemically ordered structure of B2 and $L2_1$ type. Taking into account the relative intensity of the superlattice reflections in the $[0\,1\,1]_{bcc\text{-}matrix}$ SADP (Figs. 2g and 5d), a significantly higher fraction of $L2_1$ ordering is identified in the MA_H_Al and M_H_Al alloys. The dark-field TEM micrographs shown in Figs. 2g and 5d were taken using a $L2_1$ [1 1 1] spot.

Since the average Mn content in the particles is slightly below 25 at.% (Fig. 2c) and SADP analysis revealed B2 reflections (in addition to $L2_1$ reflections) in the MA_H_Al alloy (Fig 2c), it is suggested that the $L2_1$ ordered particles also mostly contain some crystal domains where the Al/Mn atoms do not exhibit long-range ordering. The occurrence of the Al/Mn ordering defect produces intrinsic antiphase domain boundaries, such as reported in bulk Heusler-type Ni_2MnAl alloys aged at temperatures below, but close to, the B2/$L2_1$ order–disorder transition temperature [11] or in B2/$L2_1$ structured Ni_2TiAl precipitates [45].

Precipitation of the $L2_1$–Ni_2MnAl intermetallic compound was also found by Heo et al. upon ageing a Fe–8.3Mn–8.2Ni–4.2Al (wt.%) martensitic alloy at 500 °C [46]. Liebscher et al. found the formation of hierarchically structured Ni_2TiAl B2/$L2_1$ precipitates with an internal APB network in a ferritic steel [45].

6.3. Medium Al alloying

To obtain a better understanding of the interplay of NiMn and Ni_2MnAl precipitates, a nominal Al content of 0.75 wt.% (~1.5 at.%) Al has also been chosen for the MA_M_Al alloy. This value is slightly below the critical Al content predicted by ab initio calculations (Fig. 7). In this case, the TEM and APT results (Fig 2d and e) suggest that both types of ordered structures are present in similar proportions. Compared with the alloy with high Al alloying, the amount of B2 structured precipitated is substantially enhanced, as shown by the relative intensities of B2 reflexes with respect to $L2_1$ reflexes in the SADP (Figs. 2 and 5). Furthermore, the average Mn concentration of the precipitates is close to 30 at.% (Fig. 2f) indicating that both structures, Ni_2MnAl and B2–NiMn, are formed in the MA_M_Al alloy.

This observation confirms that the nominal Al content exerts a strong influence on the type of precipitates that form in maraging-TRIP steels, in quantitative agreement with the theoretical predictions.

6.4. Precipitate dispersion

It is important to note that, in the case of high Al alloying and Ni_2MnAl Heusler type precipitation, a uniform distribution of much finer precipitates (average diameter 3–5 nm) occurs compared with the case of medium and low Al alloying and NiMn precipitation (average diameter 5–10 and 10–20 nm, respectively). Simultaneously, the number density of particles is almost one order of magnitude higher in the case of MA_H_Al and M_H_Al than that obtained in the MA_L_Al and M_L_Al alloys (Figs. 2 and 5).

The differences in size and spatial distribution of the nanosized precipitates formed in the alloys can be interpreted in terms of classical nucleation theory.

The ab initio calculations (Fig. 6) yield a constrained elastic misfit parameter δ, which is defined as the relative difference of lattice constants between precipitate and matrix. Small and positive misfit parameters of 3% and 2% for B2–NiMn/α' and $L2_1$–Ni_2MnAl/α', respectively, indicate that coherent interfaces with only elastic misfit are expected in both types of precipitates embedded in the bcc α'-martensitic matrix as long as they are sufficiently small.

The formation of mainly Ni_2MnAl for the higher Al-containing alloys (MA_H_Al and M_H_Al) and the formation of NiMn for the lower Al alloyed steels (MA_L_Al and M_L_Al) were both predicted and experimentally observed. The lower misfit in the case of Ni_2MnAl is enabling a smaller critical nucleation radius according to classical nucleation theory, and this favours a finer dispersion in line with experimental observations.

It is important to note that the ab initio calculations (Fig. 7) suggest the formation of Heusler-type Ni_2MnAl precipitates only for the case of high-Al-containing alloys with 1.4 wt.%. Al, if the elastic coherency strain applies. Ostwald coarsening associated with the reduction in strain energy by introduction of misfit dislocations leading to semi- or incoherent interfaces would support NiMn formation.

Therefore, the smaller size and finer dispersion of $L2_1$–Ni_2MnAl precipitates is, on the one hand, the result of the favourable conditions for homogeneous nucleation and, on the other hand, the result of a link between precipitate phase stability and elastic coherency of the precipitates.

Another consequence of the lower chemical driving force for precipitate formation in the low-Al alloyed steel MA_L_Al is the presence of B2–Ni(Mn, Al, Ti) particles nucleated heterogeneously at dislocation lines; see Fig. 8. Both, APT and TEM measurements, reveal the existence of larger particles at dislocations that are significantly

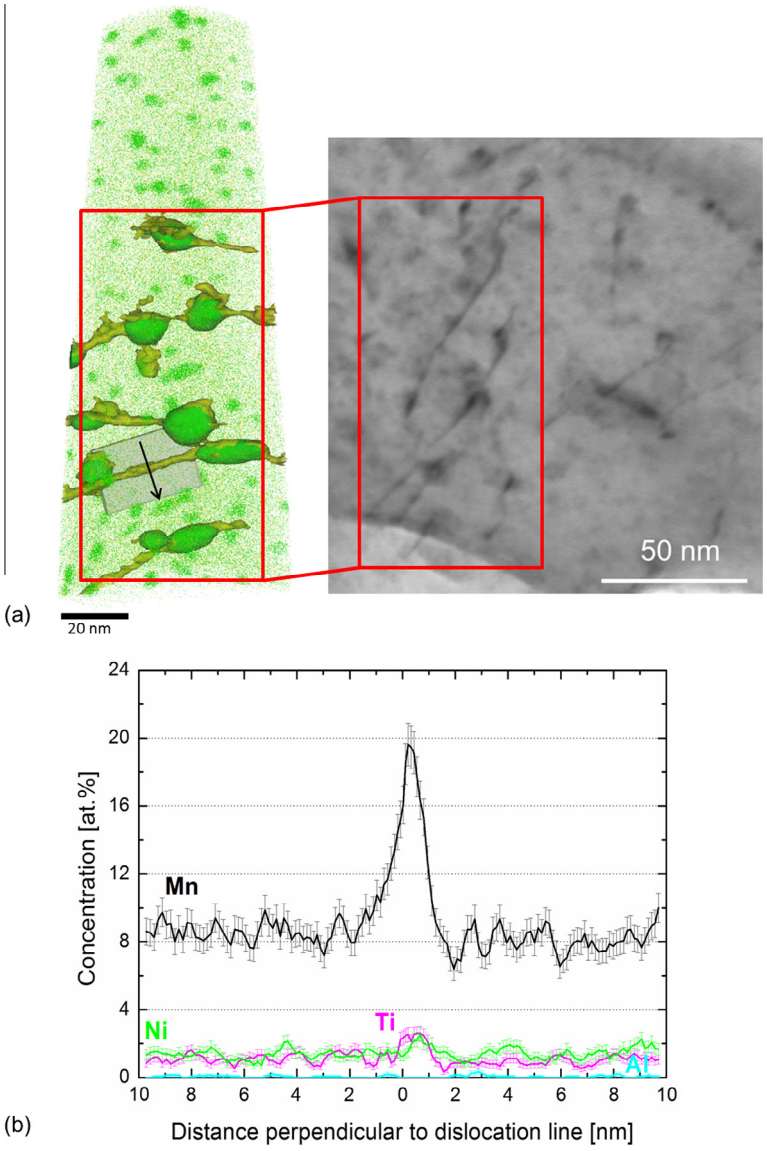

Fig. 8. (a) APT (left) and TEM (right) images showing coarser intermetallic precipitates that were formed at dislocations and not inside the defect-free regions of the bulk matrix of alloy M_L_Al after ageing at 450 °C for 65 h. In the APT reconstruction, dislocation lines in the martensite matrix are identified by a significant Mn enrichment. (b) Average chemical gradient across the dislocation line calculated via proximity histogram showing Mn enrichment (19 at.%) along the dislocation line.

enriched (19 at.%) in Mn (Fig. 8b) in the low-Al alloyed MA_L_Al and M_L_Al.

It is known that structural defects such as dislocations and grain boundaries can act as preferential sites for nucleation of precipitates. Simultaneous heterogeneous nucleation (at defects decorated with solutes) and homogeneous nucleation (inside the matrix) at small supersaturation degrees have also been observed in alloys with coherent, ordered precipitates with positive misfit parameters, such as γ'-Ni_3Al/γ_{matrix} [46,47] and Al_3Sc/Al_{matrix} [48]. Hu et al. [49] applied a phase-field model to integrate the interaction of solute fluctuations with the strain field around dislocations, showing that the nucleation of coherent precipitates at dislocations could even become nearly barrier-free. The APT reconstruction and the TEM image in Fig. 8 reveal that the particles that nucleated heterogeneously at dislocation lines are larger than those formed by homogeneous nucleation. This difference in size confirms the occurrence of fast particle growth assisted by pipe-diffusion which leads to a broader size distribution of particles in the aged M_L_Al and MA_L_Al alloys (Figs. 2, 3 and 8).

6.5. Precipitation hardening response of the fully martensitic alloys

Hardness tests on the fully martensitic references alloys, M_L_Al and M_H_Al, were performed to assess the strengthening effect of the different precipitates. The drop in hardness of the M_L_Al alloy is attributed to particle coarsening and/or to the formation of reverted austenite after a very long (~200 h) ageing time [50]. The parameters of the heat treatment evaluated in the present investigation (450 °C/65 h) still reveal an under-aged state, since the maximum peak hardness has not been reached in both alloys (Fig. 4). Therefore, it is likely that volume fraction, number density and size of the particles are still evolving, depending on the remaining supersaturation of the martensite matrix and also due to continuous Ostwald ripening.

The continuous and progressive increase in hardness of the M_H_Al alloy (Fig. 4) is associated with the formation of finely dispersed Ni_2MnAl Heusler precipitates. No incubation time is detected, indicating very fast nucleation of these precipitates. However, for the M_L_Al alloy a slight increase in hardness is seen at the beginning. Afterwards, the hardness remains approximately constant, even over a 10 h holding period. After this time, the hardness increases abruptly. The first hardening observed in alloy M_L_Al can be related to the formation of metastable Ni–Al–Mn–Ti clusters such as those reported by Pereloma et al. in a short-time-aged Ni-rich maraging steel [51] and to early precipitation via heterogeneous nucleation of the B2–Ni(Mn, Al, Ti) phase at dislocations lines (Fig. 8). The second hardening stage in the M_L_Al alloy corresponds to massive homogeneous nucleation and growth of B2–Ni(Mn, Al, Ti) particles in the martensite matrix.

The M_H_Al (Ni_2MnAl) alloy is characterised by a much finer precipitate dispersion in comparison with M_L_Al (NiMn), resulting in higher overall strengthening (Fig. 4).

In the maraging TRIP steels, MA_L_Al, MA_H_Al and MA_M_Al, the nominal Mn alloying was increased from 9 to 12 wt.% to increase the austenite stability and obtain a microstructure with a substantial portion of retained austenite after age hardening. The effect of producing such a microstructure consisting of both precipitation hardened martensite and retained austenite is an increase in ductility compared with the fully martensitic M_L_Al and M_H_Al alloys. Such alloys are hence referred to as maraging-TRIP steels [8,9].

7. Conclusions

Combined experimental and theoretical investigations were conducted on the formation of low-Ni-containing intermetallic precipitates in maraging Mn steels. The following conclusions are derived.

(i) The combined TEM and APT analysis reveals that low Al alloying (0.14 wt.% Al in MA_L_Al, M_L_Al) leads to precipitation of NiMn with B2 structured nanoprecipitates and high Al alloying (1.3 wt.% Al in MA_H_Al, M_H_Al) yields the formation of Ni_2MnAl Heusler nanoprecipitates as predicted by ab initio calculations. Medium Al alloying (0.75 wt.% Al in MA_M_Al) causes the formation of both B2 NiMn and Ni_2MnAl Heusler precipitates.

(ii) Ni_2MnAl Heusler precipitates show the smallest (3–5 nm) precipitate size and the finest dispersion in the martensitic matrix. The predominant reason for this is the smaller elastic misfit parameter and, hence, a high homogeneous nucleation rate compared with B2 NiMn.

(iii) Hardness measurements revealed a much stronger hardening effect of the M_H_Al steel, which contains Ni_2MnAl Heusler nanoprecipitates. This stronger hardening effect is related to the much finer dispersion of the Ni_2MnAl precipitates.

(iv) Ab initio predictions on phase stabilities and constrained elastic misfit parameters δ can be used to design nanoprecipitates via elastic coherency stabilization.

It was, therefore, demonstrated that the combination of ab initio calculations and high resolution microstructure characterization by TEM and APT enables the design of advanced lean maraging TRIP steels with tailored properties.

References

[1] Malakondaiah G, Srinitlas M, Rama Rao P. Prog Mater Sci 1997;42:209.
[2] Decker RF, editor. Source book on maraging steels. Metals Park, OH: ASM International; 1979.

[3] Sha W, Cerezo A, Smith GDW. Metall Trans 1993;24A:1251.
[4] Vasudervan VK, Kim SJ, Wayman CM. Metall Trans 1990;21A:2655.
[5] Servant C, Bouzid N. Acta Metall 1988;36:2771.
[6] Decker RF, Eash JT, Goldman AJ. Trans ASM 1962;55:58.
[7] Raabe D, Sandlöbes S, Millán J, Ponge D, Assadi H, Herbig M, et al. Acta Mater 2013;61:6132.
[8] Raabe D, Ponge D, Dmitrieva O, Sander B. Scr Mater 2009;60:1141.
[9] Dmitrieva O, Ponge D, Inden G, Millán J, Sietsma J, Choi P, et al. Acta Mater 2011;59:364.
[10] Potapov PL. Scr Metall Mater 1994;31:1243.
[11] Sutou Y, Ohnuma I, Kainuma R, Ishida K. Metall Mater Trans 1998;29A:2225.
[12] Miller MK, Cerezo A, Hetherington MG, Smith GDW. Atom probe field ion microscopy. Oxford: Oxford University Press; 1996.
[13] Miller MK. Atom probe tomography analysis at the atomic scale. New York: Kluwer Academic/Plenum; 2000.
[14] Seidman D. Annu Rev Mater Sci 2007;37:127.
[15] Marquis EA, Miller MK, Blavette D, Ringer SP, Sudbrack CK, Smith GDW. MRS Bull 2009;34:725.
[16] Duarte MJ, Klemm J, Klemm SO, Mayrhofer KJJ, Stratmann M, Borodin S, et al. Science 2013;341:372.
[17] Marquis A, Choi PP, Danoix F, Kruska K, Lozano-Perez S, Ponge D, et al. Microsc Today 2012;20:44.
[18] Li YJ, Choi PP, Borchers C, Westerkamp S, Goto S, Raabe D, et al. Acta Mater 2011;59:3965.
[19] Perdew JP, Burke K, Ernzerhof M. Phys Rev Lett 2004;77:3865.
[20] Kresse G, Furthmüller J. Phys Rev B 1996;54:1116.
[21] Blöchl PE. Phys Rev B 1994;50:17953.
[22] Zunger A, Wei S-H, Ferreira LG, Bernard JE. Phys Rev Lett 1990;65:353.
[23] van de Walle A, Ceder G. J Phase Equilib 2002;23:348.
[24] Von Pezold J, Dick A, Friak M, Neugebauer J. Phys Rev 2010;81B:094203.
[25] Dmitrieva O, Choi P, Gerstl SSA, Ponge D, Raabe D. Ultramicroscopy 2011;111:623.
[26] Zhang H, Punkkinen MPJ, Johansson B, Hertzman S, Vitos L. Phys Rev B 2010;81:184105.
[27] Friak M, Hickel T, Kormann F, Udyansky A, Dick A, von Pezold J, et al. Steel Res Int 2011;82:86.
[28] Reeh S, Music D, Gebhardt T, Kasprzak M, Jäpel T, Zaefferer S, et al. Acta Mater 2012;60:6025.
[29] Singh J, Wayman CM. Mater Sci Eng 1987;94:233.
[30] Squires DR, Wilson EA. Metall Trans 1972;3:575.
[31] Squires DR, Wilson FG, Wilson EA. Metall Trans 1974;5:2569.
[32] Lee H-C, Mun S-H, Mackenzie D. Metall Mater Trans 2003;34A:2421.
[33] Mun S, Watanabe M, Li X, Hwan Oh K, Williams DB, Lee H. Metall Mater Trans 2002;33A:1057.
[34] Nedjad SH, Ahmadabadi MN, Mahmudi R, Furuhara T, Maki T. Mater Sci Eng 2006;438–440A:288.
[35] Nedjad SH, Ahmadabadi MN, Furuhara T, Maki T. Phys Status Solidi (a) 2006;203:2229.
[36] Heo NH. Scr Mater 1996;34:1517.
[37] Baele I, Van Tendeloo G, Amelinckx S. Acta Metall 1987;35:401.
[38] Ding L, Ladwig PF, Yan X, Chang YA. Appl Phys Lett 2002;80:1186.
[39] Potapov PL, Polyakova NA, Udovenko VA, Svistunova EL. Z Metallk 1996;81:33.
[40] Adachi K, Wayman CM. Metall Mater Trans 1985;16A:1567.
[41] Guo Z, Sha W, Vaumousse D. Acta Mater 2003;51:101.
[42] Ping DH, Ohnuma M, Hirakawa Y, Kadoya Y, Hono K. Mater Sci Eng 2005;394A:285.
[43] Schober M, Schnitzer R, Leitner H. Ultramicroscopy 2009;109:553.
[44] Kolli RP, Mao Z, Seidman DN, Keane DT. Appl Phys Lett 2007;91:241903.
[45] Liebscher CH, Radmilovic V, Dahmen U, Asta M, Ghosh G. J Mater Sci 2013;48:2067.
[46] Heo Y-U, Takeguchi M, Furuya K, Lee H-C. J Electron Microsc 2010;59:135.
[47] Gleiter H, Hornbogen E. Mater Sci Eng 1968;2:285.
[48] Hornbogen E, Mukherjee M. Z Metallk 1964;55:293.
[49] Marquis EA, Seidman DN. Acta Mater 2001;49:1909.
[50] Hu SY, Chen LQ. Acta Mater 2001;49:463.
[51] Pereloma EV, Stohr RA, Miller MK, Ringer SP. Metall Mater Trans 2009;40A:3069.